Bulk hydrotreating MonW12-nS2 catalysts based on SiMonW12-n heteropolyacids prepared by alumina elimination method

Aleksandr Kokliukhin, Maria Nikulshina, Alexander Mozhaev, Christine Lancelot, Carole Lamonier, Nicolas Nuns, Pascal Blanchard, A. Bugaev, Pavel Nikulshin

Bulk hydrotreating $Mo_nW_{12-n}S_2$ catalysts based on $SiMo_nW_{12-n}$ heteropolyacids prepared by alumina elimination method

A. Kokliukhin[a,b,c], M. Nikulshina[a], A. Mozhaev[a,c], C. Lancelot[b], C. Lamonier[b], N. Nuns[d], P. Blanchard[b], A. Bugaev[e,f], P. Nikulshin[a,c,g*]

[a] *Samara State Technical University, 244 Molodogvardiyskaya St., 443100, Samara, Russia*

[b] *Univ. Lille, CNRS, Centrale Lille, ENSCL, Univ. Artois, UMR 8181 – UCCS – Unité de Catalyse et Chimie du Solide, F-59000 Lille, France*

[c] *Gubkin Russian State University of Oil and Gas, Leninskiy Prospect 65, 119991, Moscow, Russia*

[d] *Université Lille, CNRS, INRA, Centrale Lille, ENSCL, Univ. Artois, FR 2638 - IMEC - Institut Michel-Eugène Chevreul, F-59000 Lille, France*

[e] *The Smart Materials Research Institute, Southern Federal University, Sladkova 178/24, 344090, Rostov-on-Don, Russia*

[f] *Southern Scientific Centre, Russian Academy of Sciences, Chekhova 41, 344006, Rostov-on-Don, Russia*

[g] *All-Russia Research Institute of Oil Refining, 6 Aviamotornaya st., Moscow, 111116, Russia*

[*]Corresponding author. Tel/Fax: +7 846 2423580

E-mail: p.a.nikulshin@gmail.com (Pavel Nikulshin)

Abstract

A series of unsupported mono- and bimetallic $Mo_nW_{12-n}S_2$ catalysts were synthesized by alumina elimination from supported $Mo_nW_{12-n}S_2/Al_2O_3$ samples using acid etching. Alumina supported catalysts have been in turn prepared by using monometallic $H_4SiMo_{12}O_{40}$ and $H_4SiW_{12}O_{40}$ heteropolyacids (HPAs), their mixture with Mo/W atomic ratio equal to 1/11 and 3/9,

and mixed bimetallic $H_4SiMo_1W_{11}O_{40}$ and $H_4SiMo_3W_9O_{40}$ HPAs. All catalysts were characterized by N_2 adsorption, temperature-programmed reduction (TPR), X-ray photoelectron spectroscopy (XPS), high-resolution transmission electron microscopy (HRTEM), time-of-flight secondary ion mass spectrometry (ToF-SIMS), extended X-ray absorption fine structure (EXAFS) spectroscopy and powder X-ray diffraction (XRD) and their performance were evaluated in simultaneous hydrodesulfurization (HDS) of dibenzothiophene (DBT) and hydrogenation (HYD) of naphthalene. The etching process led to a successful removal of all the support and of the partially sulfided species, with sulfidation degrees of both Mo and W above 90% on the final bulk solids. The active phase also underwent a rearrangement, as higher average length and stacking were measured on the bulk catalysts than on the original supported ones. Mixed $MoWS_2$ phase was evidenced in all solids, prepared from mixed HPAs ($Mo_nW_{12-n}S_2$) or from the mixture of monometallic HPAs ($RefMo_nW_{12-n}S_2$), by EXAFS and ToF-SIMS, with however a larger quantity on the MoW solids. It seems that the mixed $MoWS_2$ phase observed on the supported MoW catalysts is maintained through the etching process, while on $RefMo_nW_{12-n}S_2$ the mixed phase, observed in a much lesser extent in the corresponding supported catalyst, could result from the aggregation of the monometallic slabs. $Mo_nW_{12-n}S_2$ catalysts were found more effective than the monometallic catalysts and than the corresponding $RefMo_nW_{12-n}S_2$, in both dibenzothiophene hydrodesulfurization and naphthalene hydrogenation, which was related to the presence of the mixed phase maintained through the etching of the support.

Keywords: Hydrodesulfurization; Heteropolyanion; $MoWS_2$ catalysts; Unsupported catalyst, DBT, Naphthalene, EXAFS.

1. Introduction

Due to stricter environmental standards, the oil industry is under pressure to provide clean fuels. Therefore, in recent years, special attention has been focused on improving the activity and stability of hydrotreating catalysts for petroleum fractions. Mixed NiMoW sulfides based on

alumina [1-4], silica [5] or mesostructured silica [6] demonstrated excellent catalytic activity in hydrodesulfurization (HDS) of sulfur compounds. The superiority of mixed NiMoW systems over traditional bimetallic Ni(Co)Mo(W) catalysts was attributed to the synergistic effect when using Ni, Mo and W. With the density functional theory (DFT) calculations, it was found that NiMoWS catalysts have a more optimal metal-sulfur bond energy compared to NiMoS and NiWS catalysts [2].

The use of Ni(Co)MoWS systems, in which both tungsten and molybdenum atoms are simultaneously present, allowed increasing HDS and HYD activities [1-3,7-10]. Thomazeau et al. [2] reported that the formation of mixed $MoWS_2$ crystallites is possible only from a precursor which contains both closely related metals in the structure at once. The structure of the mixed active phase is greatly influenced by sulfidation conditions. Previously, for unpromoted catalysts based on mixed $H_4SiMo_3W_9O_{40}$ heteropolyacid (HPA), we found that mixed $MoWS_2$ active species with a core-shell structure, in which smaller islands of Mo were surrounded by W atoms, were formed in the gas-phase sulfidation, while in the liquid-phase sulfidation a structure with random distribution of molybdenum and tungsten atoms was formed, as visualized by HAADF [11]. Moreover, it was found that the use of a mixture of two monometallic $H_4SiMo_{12}O_{40}$ and $H_4SiW_{12}O_{40}$ HPAs led to the preferential formation of corresponding monometallic MoS_2 and WS_2 particles. In the co-hydrotreatment of DBT and naphthalene, catalysts with an ordered core-shell structure of the $MoWS_2$ active phase had highest rate constants for both HDS and HYD reactions.

In addition, the possibility of using bulk Mo(W) sulfide catalysts, which do not contain a support, in hydrotreatment processes on stationary catalyst beds is also being investigated. The concentration of active phase in these catalysts can reach 80-100%. With the same composition of the active phase, the activity of bulk catalysts in hydroprocessing can be 1.5–1.7 times higher than that of their supported analogs. Thus, industrial bulk NiMoW NEBULA catalysts have higher catalytic activity compared to traditional alumina supported catalysts. The increase in catalytic activity can be explained by the formation of highly active trimetallic NiMoW sulfides [12]. In the

middle of last year, the ExxonMobil jointly with Albemarle proposed a new catalyst, Celestia™, the successor of the NEBULA catalyst. Industrial implementation makes promising the development of new catalytic systems based on bulk mixed NiMoW sulfides.

Recently, due to the development of technologies for deep hydroconversion of heavy oil residues in three-phase suspension-type reactors (slurry-reactors) [13-16], in which nanoscale (Ni)Mo(W)S_2 particles are formed *in situ* [14-16], the interest to bulk catalysts based on transition metal sulfides, has been increasing.

Various methods for preparing bulk catalysts such as comaceration [17], homogeneous sulfide precipitation [18], thiosalt decomposition [19], hydrothermal [20-21] and solvothermal [22-23] syntheses, as well as the method of fluoric acid (HF) etching of the substrate of supported catalysts [24-25] have been described. Previously, we reported that unsupported catalysts synthesized *via* etching of alumina support, exhibited higher catalytic properties compared to those prepared by other methods [26], due to high dispersion of active sulfide particles and good accessibility to active sites.

Summarizing the above, it seems appropriate to combine the method of HF etching of a support and the use of mixed MoW oxide precursors to produce mixed bulk catalysts. That will allow purposefully creating catalysts with a given composition of mixed $MoWS_2$ particles. In the present work, mixed MoWS bulk catalysts were synthesized by acid etching of alumina support from supported sulfide catalysts based on mixed $H_4SiMo_1W_{11}O_{40}$ and $H_4SiMo_3W_9O_{40}$ HPAs. Catalysts prepared from mixture of two monometallic $H_4SiMo_{12}O_{40}$ and $H_4SiW_{12}O_{40}$ HPAs with the same Mo/W molar ratio as in corresponding mixed HPAs were used as reference samples. The effects of catalyst composition on catalytic performance were studied in the hydrotreating reactions of DBT and naphthalene. Prepared bulk catalysts were characterized by methods such as nitrogen physisorption, extended X-ray absorption fine stricture spectroscopy (EXAFS), transmission electron microscopy (TEM), X-ray photoelectron spectroscopy (XPS), time-of-flight secondary ion mass spectrometry (ToF-SIMS) and powder X-ray diffraction (XRD). Moreover, a

comparison was made with their alumina supported counterparts in order to reveal the effect of the support.

2. Experimental

2.1. Catalyst preparation

A series of bulk $Mo_nW_{12-n}S_2$ hydrotreating catalysts was synthesized by HF etching of alumina from Mo_nW_{12-n}/Al_2O_3 catalysts. First, supported samples were prepared by the incipient wetness method via impregnation of γ-Al_2O_3 extrudates with aqueous solutions of $H_4SiMo_nW_{12-n}O_{40}$ HPAs [4,9-11]. These mixed HPAs are derived from the Keggin-type polyoxometallate $H_4SiW_{12}O_{40}$, consisting of a regular SiO_4 tetrahedron surrounded by 12 WO_6 octaedra, which are connected by shared edges to form trimetallic W_3O_{13} groups joined together by their vertices. Replacement of one or 3 W atoms by Mo led to the formation of α-$H_4SiMo_1W_{11}O_{40}$ and β-$H_4SiMo_3W_9O_{40}$ HPAs, the structure and synthesis methodology of which were described earlier by Nikulshina et al. [9]. Two catalysts were synthesized using mixed Keggin-type α-$H_4SiMo_1W_{11}O_{40}$ and β-$H_4SiMo_3W_9O_{40}$ HPAs (named as $Mo_1W_{11}S_2$ and $Mo_3W_9S_2$, respectively), another two were based on monometallic $SiMo_{12}$ and SiW_{12} HPAs (named as MoS_2 and WS_2, respectively), and finally two more bimetallic MoW reference samples were synthesized from a mixture of monometallic HPAs with Mo/W ratios of 1/11 and 3/9 (denoted $RefMo_1W_{11}S_2$ and $RefMo_3W_9S_2$, respectively). The oxidic dried samples were sulfided in a fixed-bed reactor at 400 °C for 4 h in a stream of 10 vol. % of H_2S in H_2 under atmospheric pressure. Detailed characterization of the prepared supported catalysts was described in [9,11]. After sulfidation, the samples were treated by a solution of hydrofluoric acid. A typical HF etching process was carried out as follows [24]: 10 g of sulfided Mo_nW_{12-n}/Al_2O_3 catalyst, 215 g of 45 wt. % HF, and 537 ml of deionized water were added to a plastic beaker. Required amounts of HF were calculated to have a molar ratio HF/ Al_2O_3 of 60. This mixture was kept with magnetic stirring at 40 ºC for 4 h to form a black suspension. The solid material was then filtered, washed with 50 ml of deionized water and acetone, dried in rotary evaporator under vacuum. The chemical compositions of the prepared catalysts are given in **Table 1**. Content of carbon and sulfur was measured using 2400 Series II CHNS elemental analyzer. Amount of metals was determined using EDX-7000P XRF analyzer. Prior the characterization of the active phase of the catalysts and evaluation of their catalytic activities, the solids were sulfided according to the method described above.

2.2. Characterization of the catalysts

2.2.1. Textural properties of catalysts

Textural characteristics of the alumina supported sulfides and solids after HF etching were determined by N_2 physisorption at 77 K on a Quantochrome Autosorb-1 adsorption porosimeter. The samples were outgassed under vacuum at 623 K for 6 h prior to the adsorption. Specific surface areas were calculated using the BET method at a relative partial pressure $P/P_0 = 0.05–0.3$. Total pore volumes were determined by a desorption curve using the BJH model at a relative partial pressure $P/P_0 = 0.99$. Pore size distributions were calculated using DFT analysis.

2.2.2. TPR

H_2-TPR of the sulfided samples was carried out on a TPDRO 1100 apparatus with the use of a thermal conductivity detector. Analysis was held in a mixture of H_2 and N_2 (5 vol. % of H_2) under the following conditions: volume flow rate of 25 ml/min, temperature range from room temperature to 900 ºC, heating rate of 10 ºC /min.

2.2.3. HRTEM

The morphology of the prepared samples was investigated by means of HRTEM. HRTEM measurements were performed using a Tecnai G2 20 microscope with a 0.14 nm lattice-fringe resolution and an accelerating voltage of 200 kV. For statistical analysis, slab length and layer stacking of 400-600 $Mo_nW_{12-n}S_2$ crystallites were determined for each catalyst.

The average length ($\bar{L}$) was calculated as an arithmetic mean and corresponds to the average dimension of the projection of the slabs parallel to the electron beam [26]. The number of slabs per stack was determined to obtain the average stacking degree ($\overline{N}$):

$$\overline{N} = \frac{\sum_{i=1..t} n_i N_i}{\sum_{i=1..t} n_i}, \quad (1)$$

where n_i is the number of stacks with N_i slabs.

The dispersion of Mo(W)S_2 species was evaluated statistically by dividing the total number of Mo(W) atoms on the edge by the total number of Mo(W) atoms using crystallite sizes determined from HRTEM, which is a common method for determining metal sulfides dispersion for supported [27,28] and bulk [29,30] catalysts. It is assumed that during sulfidation ideal hexagonal particles are formed.

2.2.4. Powder XRD

Powder XRD data collection was performed on an ARLX'TRA diffractometer with Cu Kα emission (λ = 1.54056 Å) operating at 43 kV and 38 mA and recorded peaks were identified using standard JCPDS files. The approximate crystallite dimensions of the MoS_2 slabs were calculated using the Debye-Scherrer relation [31]:

$$D_{002} = \frac{k_{002} \cdot \lambda}{\beta_{002} \cdot \cos\theta} \quad (2)$$

where D_{002} is the mean size of ordered (crystalline) domains (Å) along the stacking direction; λ is the X-ray wavelength; θ is the Bragg angle; β_{002} (or FWHM) is the line broadening at half maximum intensity; k_{002} is the dimensionless shape factor. The shape factor k_{002} depends on the crystal shape and is close to 0.9 for WS_2 [32] and to 0.76 for MoS_2 [31]. The average number of layers N was calculated using the equation $N = D_{002}/6.17$, where 6.17 Å corresponds to the value of the interlayer spacing in the 2H-WS_2 structure.

The crystallite size along the basal direction was calculated using the Debye-Scherrer equation (2) applied to the broadening of the diffraction peak (110). The same calculation method was previously used by de la Rosa et al. [31] for MoS_2 prepared by HF acid etching of the support. The peak (110) is not affected by imperfect stacking or bending/folding of layers [31,33]. However, Liang et al. [33] found that the shape factor k_{110} depends on the β_{110} angular line width, and this correlation between β_{110} and k_{110} was taken into account. According to the experimental angular line widths, the shape factor k_{110} was equal to 1.49.

2.2.5. XPS

XPS experiments were performed on a KRATOS Axis Ultra spectrometer with a monochromatic Al K_α source ($h\nu$ = 1486.6 eV, 150 W). The binding energy (BE) values were referred to C1s at 284.8 eV to account for charging effects [34]. The spectrum decomposition was carried out using Casa XPS software after applying a Shirley background subtraction and using Gaussian–Lorentzian (30/70) parameters. S2p, Mo3d, W4f, C1s and O1s spectra were collected. The relative concentrations of each species Mo^{6+}, Mo^{5+} (MoS_xO_y), Mo^{4+} (MoS_2) on Mo3d region (analogically for W_{4f}) were determined for all sulfided catalysts. The relative amounts of metal fractions were determined according to previous works [11, 35, 36].

2.2.6. EXAFS spectroscopy

The Mo *K*-edge and W $L_{1,2,3}$ -edges EXAFS spectra were collected at BM31 beamline of the ESRF (Grenoble, France) [37]. The sample powder was diluted with boron nitride, pressed into a pellet and sealed with Kapton tape. All spectra were recorded at room temperature in transmission mode with simultaneous collection of molybdenum and tungsten metal foils for energy calibration. The energy was selected with a double-crystal Si (111) monochromator in the continuous scanning mode. EXAFS data analysis (normalization, background removal, energy alignment, extraction of $\chi(k)$ signal and Fourier analysis) was performed in the Demeter software package [38], FEFF6 [39] was used to calculate theoretical phases and amplitudes. The following structural parameters were set as variables during the fit: interatomic distances (R), coordination numbers (N), Debye-Waller factors (σ^2) for Mo–Mo, Mo–S, Mo–W (and W–Mo), W–W, and W–S scattering paths. To reduce the number of variables, R and σ^2 for W–Mo path were set equal to the corresponding values of Mo–W path. The equation $N_{\mathrm{W-Mo}} = \frac{N_{\mathrm{Mo-W}}}{3}$ was also applied, based on the stoichiometric ratio of the two metals. Two energy shifts (ΔE_0) were used for all paths at Mo *K*- and L_3-edges The fit was performed in R-space in 1.2 - 3.4 Å range using a multiple k-weighted data (1,2,3). The Fourier-transformation ranges for Mo *K*-edge and W L_3-edge were set to Δk_K = 3.5-15.0 $Å^{-1}$, Δk_{L3} = 4.3-16.3 $Å^{-1}$, respectively. Amplitude reduction factors (S_0^2) were obtained by fitting bulk MoS_2 and

WS_2 references. For direct comparison, the same fitting strategy was applied for the analysis of the data previously collected for the supported catalysts [9].

2.2.7. ToF-SIMS measurements

ToF-SIMS measurements were performed with a TOF.SIMS 5 spectrometer (ION-TOF GmbH Germany) equipped with a bismuth liquid metal ion gun (LMIG). The compacted samples were bombarded with pulsed Bi^{3+} primary ion beam (25 keV, 0.25 pA) rastered over a 100 × 100 m^2 surface area. With 30 scans and 128x128 pixels, the total primary ion dose does not amount up to 1012 ions/cm^2 ensuring static conditions. Charge effects due to primary ion beam were compensated by means of a 20 eV pulsed electron flood gun. Cycle time was fixed at 150 µs in order to detect secondary molecular ions up to 2000 m/z. The mass resolution (m/Δm) measured on our spectra was about 4000 at m/z = 143 for MoO_3^-. This good mass resolution allowed us to identify high m/z ionic fragments by their exact mass and the attribution could be confirmed most of the time by the simulated isotopic pattern.

2.3. Catalytic performances

The HDT activity tests were performed in a bench-scale flow reactor at 320 ºC, 3.0 MPa total pressure of hydrogen, with a liquid hourly space velocity (LHSV) of 40 h^{-1} and a 500 NL/L volume ratio of hydrogen to feed. Pre-sulfided $Mo_nW_{12-n}S_2$ catalysts (0.2 g) were diluted with 0.6 cm^3 of low-surface-area carborundum (0.2–0.4 mm) and placed in the center of the reactor with an internal diameter of 0.8 cm. A toluene solution of DBT (Aldrich, 1500 ppm of S), naphthalene (Aldrich, 3wt. %) and hexadecane (as an internal standard, 1 wt. %) was used as a model feedstock. The liquid product compositions of the samples collected every hour were determined using a Crystall-5000 Gas Chromatograph equipped with a 30 m OV-101 column. The reaction products were identified by matching retention times with those of commercially available standards and by GC/MS analysis using a Finnigan Trace DSQ. All catalysts exhibited stable performance, achieving a steady state after 7 – 10 h.

The rate constants of the pseudo-first-order reactions of the DBT HDS and naphthalene HYD were determined using the following equations:

$$k_{\mathrm{HDS}} = -\frac{F_{\mathrm{DBT}}}{W}\ln(1 - x_{\mathrm{DBT}}) \text{ and } k_{\mathrm{HYD}} = -\frac{F_{\mathrm{Naph}}}{W}\ln(1 - x_{\mathrm{Naph}}), \quad (3)$$

where k_{HDS} and k_{HYD} are the pseudo-first-order reaction constants for the DBT HDS and naphthalene HYD (mol g^{-1} h^{-1}), respectively, x_{DBT} and x_{Naph} are the conversions (%) of DBT, and naphthalene, respectively, F_{DBT} and F_{Naph} are the reactant flows in moles (mol h^{-1}) and W is the weight of the catalyst (g).

The HDS products from DBT included biphenyl (BP) via the direct desulfurization (DDS) pathway, as well as cyclohexylbenzene (CHB) and dicyclohexyl (DCH) from the HYD pathway. Only traces of hydrogenated tetrahydro- and hexahydrodibenzothiophenes were observed. The HYD/DDS selectivity was calculated according to the reaction network for DBT HDS:

$$S_{HYD/DDS} = \frac{k_{\mathrm{HYD}}}{k_{\mathrm{DDS}}} = \frac{C_{\mathrm{CHB}} + C_{\mathrm{DCH}}}{C_{\mathrm{BP}}} \quad (4)$$

where C_{CHB}, C_{BCH} and C_{BP} are the concentrations (mol. %) of CHB, DCH and BP in the reaction products, respectively.

The turnover frequencies (TOF, s^{-1}) normalized on edge sites of $Mo_nW_{12-n}S_2$ slabs for the HDS of DBT, HYD of naphthalene allowed us to get more complete understanding of the catalytic properties of the active phase species. TOF values were calculated using the following equations:

$$TOF_{\mathrm{HDS}} = \frac{F_{\mathrm{DBT}} \cdot x_{\mathrm{DBT}}}{W \cdot \left(\frac{C_{\mathrm{WS_2}}}{Ar_{\mathrm{W}}} + \frac{C_{\mathrm{MoS_2}}}{Ar_{\mathrm{Mo}}}\right) \cdot D \cdot 3600} \text{ and } TOF_{\mathrm{HYD}} = \frac{F_{\mathrm{Naph}} \cdot x_{\mathrm{Naph}}}{W \cdot \left(\frac{C_{\mathrm{WS_2}}}{Ar_{\mathrm{W}}} + \frac{C_{\mathrm{MoS_2}}}{Ar_{\mathrm{Mo}}}\right) \cdot D \cdot 3600}, \quad (5)$$

where F_{DBT} and F_{Naph} are the reactant flows (mol h^{-1}), x_{DBT} and x_{Naph} are the conversions (%) of DBT and naphthalene, respectively; W is the weight of the catalyst (g); $C_{\mathrm{WS_2}}$ and $C_{\mathrm{MoS_2}}$ are the effective content of W and Mo, respectively, in $Mo_nW_{12-n}S_2$ species (wt. %); D is the dispersion

of $Mo_nW_{12-n}S_2$ species; Ar_W and Ar_{Mo} are the standard atomic weights of tungsten (183.9 g/mol) and molybdenum (95.9 g/mol), respectively.

3. Results

3.1. Textural properties of catalysts

The textural properties of the prepared samples are summarized in **Table 1**. Sulfided alumina-based precursors displayed surface areas in the range of 164 to 218 m^2/g and pore volumes around 0.53 cm^3/g. The alumina removal resulted in a decrease of the surface area to 3-14 m^2/g and pore volume to 0.01-0.04 cm^3/g. These significant changes in the textural properties are related to the total removal of the porous support. X-ray fluorescence and XPS analysis confirmed the absence of aluminum and silicon in the solids after etching procedure. According to Fig. 1S, all materials exhibit adsorption isotherms similar to type I with virtually a non-porous structure. These results are in agreement with those previously reported for bulk catalysts [40-43].

3.2. TPR analysis

Fig. 1 shows the H_2-TPR profiles of the unsupported $Mo_nW_{12-n}S_2$ catalysts and of their references. The reduction of the MoS_2 sample proceeded in the region 100-400 ºC with a maximum at 303 ºC. The TPR profiles of WS_2 displayed two reduction regions: 250-400 ºC (T_{max}=342 ºC) and 400-600 ºC (T_{max}=461 ºC). The appearance of a peak in the high-temperature region for WS_2 can be attributed to stronger W–S bond than Mo–S [44]. All bimetallic catalysts also exhibited two main reduction peaks. According to the literature [45-47], the first low-temperature peak corresponds to surface weakly bonded sulfur. Afanasiev et al. [46] believe that after the reduction of surface sulfur, coordinative unsaturated sites (CUS) are formed, which in turn are responsible for the reactions that occur on the surface of the catalyst. This allows to indirectly estimate the possible number of active sites. Lower reduction temperatures of mixed HPA based catalysts are observed compared to that of their corresponding references: 334 and 378°C for $Mo_1W_{11}S_2$ and its

reference, 319 and 339°C for $Mo_3W_9S_2$ and its reference for the first reduction peak. This can be related to a decrease in the strength of the metal-sulfur bond due to the formation of mixed $MoWS_2$ particles with a more optimal bond energy value [48]. As the molybdenum loading increased, the reducibility of the catalysts was enhanced as indicated by the decrease in the reduction temperature (342°C for WS_2, 334°C for $Mo_1W_{11}S_2$, 319°C for $Mo_3W_9S_2$) and the increase in H_2 consumption (230 mmol/mol for WS_2, 390 mmol/mol for $Mo_1W_{11}S_2$, 640 mmol/mol for $Mo_3W_9S_2$, **Table 2**). Furthermore, the H_2 consumption was higher for the samples based on MoW HPAs than for their analogs prepared from a mixture of separate HPAs (390 and 367 mmol/mol for $Mo_1W_{11}S_2$ and its Ref, 640 and 450 mmol/mol for $Mo_3W_9S_2$ and its Ref), which indicates that a larger amount of active sites is present in the $Mo_nW_{12-n}S_2$ catalysts.

The maxima temperature of the first reduction peak was lower in the supported catalysts than in the corresponding bulk ones after HF etching. H_2 consumption of all tungsten-containing catalysts was higher than the values of corresponding alumina supported samples (**Table 2**), which can be related to a larger amount of active sites through increasing the number of $Mo(W)S_2$ species.

3.3. Morphology of the active phase

Morphology of $Mo_nW_{12-n}S_2$ particles was investigated by HRTEM. **Fig. 2** shows representative TEM images taken for bulk samples. Typical fringes of $Mo(W)S_2$ crystallites with 6.1 Å interplanar distances were observed on micrographs of all sulfided catalysts. Average length and stacking of bulk $Mo_nW_{12-n}S_2$ catalysts are shown in **Table 3**. Monometallic WS_2 catalyst had the highest average length (6.7 nm) and stacking (3.5) among all the prepared samples. MoS_2 species of pure molybdenum catalyst were shorter (5.2 nm) and a little less stacked than those of pure tungsten disulfide one. Addition of molybdenum atoms in the content of the catalysts resulted in a decrease in size of sulfided slabs. Both bimetallic reference catalysts had almost the same average length despite different Mo contents, while the particles size decreased with the increase of Mo amount in mixed HPAs based catalysts. All bimetallic samples had an average stacking around 3.0, which expectedly exceeded the values for conventional supported catalysts with 1-2

stacking layers [49,50]. Therefore, removing of the alumina support led to agglomeration of $Mo(W)S_2$ species and to reduction of their dispersion compared to initial supported ones.

3.4. XRD

The XRD patterns of the prepared $Mo_nW_{12-n}S_2$ catalysts are given in **Fig. 3**. All samples exhibited several well-resolved XRD peaks at 14 (002), 33 (100), 40 (103), and 59° (110) 2θ corresponding to MoS_2 (WS_2) structure. It can be seen that the results of XRD do not allow to identify a difference in the structure of prepared bimetallic catalysts due to slight shifts of the reflections between MoS_2 and WS_2 phases. Average crystallite sizes were estimated by Debye-Scherrer equation (**Table 3**). Monometallic references WS_2 and MoS_2 catalysts had the longest and the shortest sulfide slabs, respectively, as observed by HRTEM. Average length and stacking of crystallite in both mixed HPAs based samples and $RefMo_1W_{11}S_2$ were equivalent and less than those of WS_2. In contrast, the values calculated for $RefMo_3W_9S_2$ were close to MoS_2 catalyst. Such decrease of particles size indicated that the sample prepared from two HPAs may have separate monometallic MoS_2 and WS_2 species. In addition, it should be noted that, on the one side, a slight difference in the cell parameters of MoS_2 and WS_2 phases may also result in increasing the width of XRD peaks, leading to an underestimated value of the particle size, and on the other side, TEM results are weighted by the number of particles, while XRD is weighted by particle volume, i.e. larger particles give more contribution.

3.5. Sulfidation of metals evaluated by XPS

Fig. 4 shows examples of decomposition of Mo 3d and W 4f XPS spectra of the sulfided $Mo_nW_{12-n}S_2$ catalysts. The Mo spectra exhibit a Mo $3d_{5/2}$ peak at about 229.0 eV characteristic of MoS_2 [4,34,35,51], the W 4f spectra contain $4f_{5/2}$ peak at about 32.4 eV, associated with WS_2 [4,11,50,52].

Table 4 gives the metal fractions of molybdenum and tungsten species present on the surface of the synthesized $Mo_nW_{12-n}S_2$ catalysts. All studied samples had a high sulfidation degree of

metals (92 rel. % and more), corresponding to an increase of around 8% for Mo and more than 30% for W compared to supported catalysts [11]. That high amount of metals in the Mo(W)S_2 phase and the near absence of oxide and oxysulfide species is the result of HF etching, where only fully sulfided species were resistant. Surface Mo/W ratios were close to the bulk values determined by XRF analysis due to homogeneous distribution of particles in bulk solids. Higher Mo/W atomic ratios were detected in bulk sulfide solids compared to supported precursors. This result can be explained by the higher percentage of tungsten oxide and oxysulfide species compared to molybdenum ones contained in sulfided Mo(W)/Al_2O_3 catalysts [11], that were completely dissolved during the HF treatment. The S/metal atomic ratios for all catalysts were close to the theoretical value of 2 expected for MoS_2/WS_2.

3.6. EXAFS analysis

Fig. 5 compares the magnitude of k^3-weighted Fourier transformed (FT) EXAFS data for both unsupported and supported [9] $Mo_nW_{1-n}S_2$ catalysts (solid and dashed lines, respectively). The spectra of all catalysts exhibit two main peaks at ca. 2.0 Å and 2.9 Å (phase-uncorrected) corresponding to metal-sulfur (M–S) and metal-metal (M–M) scatterings, respectively. The shape of FT EXAFS spectra of the $Mo_nW_{1-n}S_2$ catalysts depends on the starting oxide precursor. In both Mo *K* and W L_3-edge spectra, the highest peak intensity in the region of 3 Å (phase-uncorrected) was observed for monometallic MoS_2 and WS_2 catalysts, while this intensity was lower in bimetallic samples, especially in the case of the catalyst based on the mixed $SiMo_3W_9$ HPA. This fact is indicative of the presence of two different metal-metal contributions (homo- and heterometallic) in the second coordination shell. Indeed, the W–W (Mo–Mo) and W(Mo)–Mo(W) contributions have similar frequencies, but are out of phase and cancel each other, which leads to a decrease in the amplitude of the resulting $\chi(k)$ and $\chi(R)$ signals as shown in Fig. S3. The same effect leads to a high uncertainty in the determination of the total Mo–M and W–M coordination numbers, which was overcome by fixing $N_{\mathrm{W-Mo}} = \frac{N_{\mathrm{Mo-W}}}{3}$, based on the stoichiometric ratio of

the two metals. The detailed description of the fitting procedure used to reduce the number of independent variables and to improve the fit stability is given in the Supporting Information.

The obtained best-fit values are listed in **Table 5**. All catalysts have relatively high sulfidation degree with $N_{M\text{-}S}$ ~ 5 – 6 depending on the sample. The second shell of monometallic samples contains one M–M contribution at 3.16 Å: Mo–Mo in MoS_2 ($N_{Mo\text{-}Mo}$ = 3.7) and W–W in WS_2 ($N_{W\text{-}W}$ = 4.4). The coordination numbers M–M in bimetallic catalysts depend on the initial precursor. At both Mo *K*- and W L_3-edges, $N_{M1\text{-}M2}$ (where M1 and M2 correspond to different types of metal atom) is higher in the mixed HPA based catalyst than in its bimetallic reference, which evidences the formation of a bimetallic $MoWS_2$ phase. Reference bimetallic samples also contain a mixed M1-M2 contribution, but the corresponding coordination numbers are very close to the experimental uncertainty. To highlight the structural changes induced by the elimination of the support, the corresponding values for the supported catalyst [9] analyzed using the same fitting model are reported in brackets.

3.7. ToF-SIMS analysis

Two zones were analyzed by ToF-SIMS on Mo_1W_{11} and Mo_3W_9 as well as on their reference counterparts $RefMo_1W_{11}S_2$ and $RefMo_3W_9S_2$. This technique allows to investigate possible interaction between Mo and W, as it probes the top layers (1-3 nm) of the catalysts and gives molecular information about surface and interfaces. $Mo_xO_yS_z^-$ and $W_xO_yS_z^-$ monometallic fragments were indeed recorded on pure MoS_2 and WS_2 (**Fig. 6**). On the mixed catalysts, in addition to these monometallic fragments, mixed fragments containing Mo and W are also evidenced (**Fig. 6 and Fig. S4**). These fragments clearly show that a close interaction exists between Mo and W in the bulk catalysts, indicating that the mixed $MoWS_2$ phase evidenced in the supported catalysts is maintained after etching of the support. The intensity of each identified mixed oxide fragments was normalized in order to compare the four catalysts, as illustrated in **Fig. 7**. Normalization was performed using fragment intensity of $^{182}WS^-$. If mixed fragments are obtained on all the samples, the intensity of the corresponding peaks is higher on the catalysts

prepared from mixed $SiMo_nW_{12-n}$ HPA compared to those prepared from a mixture of monometallic HPAs, as observed on the corresponding supported catalysts.

3.8. Catalytic performances

Catalytic behavior of the synthesized $Mo_nW_{12-n}S_2$ catalysts was evaluated in simultaneous HDT of two model compounds, DBT and naphthalene (**Table 6**). The results indicated that, under the chosen reaction conditions, substitution of one or three tungsten atoms by molybdenum in the catalyst composition resulted in an increase in HDS as well HYD activities compared to monometallic MoS_2 and WS_2 references, regardless of the precursor type. HDS activities in the two catalysts with Mo/W ratio = 1/11 were close. However, the $Mo_3W_9S_2$ catalyst prepared from the mixed $SiMo_3W_9$ HPA has a twice-higher catalytic activity than its $RefMo_3W_9S_2$ counterpart prepared from mixture of two separate HPAs in both studied reactions (conversions of 50 and 29% respectively in HDS and conversions of 35 and 18% respectively in HYD). These results clearly show the advantage of using the mixed $SiMo_3W_9$ HPA as the starting oxidic precursor for the synthesis of bimetallic bulk $MoWS_2$ catalyst.

The detailed analysis of the reaction products shows that for all studied catalysts, the preferential pathway in DBT HDS is pre-HYD. Selectivity HYD/DDS ratio of the prepared catalysts ranges from 1.0 to 2.8.

4. Discussion

In order to gain a better understanding of the synergetic effect between molybdenum and tungsten, the rate constants in HDS and HYD were calculated by additive way based on the results obtained over monometallic MoS_2 and WS_2 references catalysts. Experimental values of the rate constants in DBT HDS and naphthalene HYD over $Mo_1W_{11}S_2$ and $Mo_3W_9S_2$ surpass the theoretical ones by 1.4 and 2.7 times, respectively. Catalytic activities of bimetallic reference samples are also higher than predicted, however, the difference is smaller.

A comparison of catalytic properties of unsupported and alumina based catalysts shows that alumina etching results in an increase of total HDS and HYD activity that can be attributed to the absence of metal-support interaction and, as a consequence, raise of metal sulfidation degree (**Fig. 8**). It should be noted that in case of bulk catalysts, the WS_2 sample based on monometallic SiW_{12} HPA demonstrated improved catalytic properties compared to monometallic MoS_2 one. We suggest that there are two possible reasons for this effect: (i) more significant concentration of sulfide species (WS_2) in W-based catalyst during support removing due to dissolution of low active in catalysis oxide and oxysulfide particles contained in a larger amount in W-based catalyst compared to Mo-based one; (ii) more covalent W–S strength in bulk WS_2 sample due to the absence of oxysulfide species compared to supported WS_2/Al_2O_3 analog.

HF acid treatment of alumina supported sulfide catalysts leads to an increase in the linear size and average stacking number of sulfide particles, which is independently confirmed by HRTEM, XRD and EXAFS data. The metal sulfidation degree was also raised especially for tungsten, due to removal of non sulfided species. Moreover, the above results allow us to suppose that the nature of starting oxidic precursor influences the active phase composition and properties. We previously reported the formation of mixed $MoWS_2$ particles with core-shell structure, with Mo atoms predominantly located together in the core region, in Mo_3W_9/Al_2O_3 catalyst during gas phase sulfidation [9,11]. This fact is confirmed by higher total Mo–M coordination numbers in both supported and unsupported catalysts, compared to those for W–M contribution. Moreover, the changes in coordination numbers after the elimination of the support (see Table 5) indicate that the increase in Mo–Mo coordination numbers is more significant than the increase in Mo–W ones, which means that the agglomeration of MoWS slabs preferentially occurs via Mo edges as schematically illustrated in the Fig. 9a. It should be noted, that for unsupported catalyst the total Mo–M coordination numbers are close to 6 as in the bulk samples, suggesting that most of molybdenum is located inside the slabs and not on the edges.

The preferential location of Mo-atoms in the core-region of the slabs is also confirmed by Mo–S coordination numbers close to 6. The lower values obtained for W–S contribution can be explained by the elongation of W–S distances for two sulfur atoms located at M-edge, which may lead to a partial antiphase of the resulting signals, which cannot be reproduced by using a single M–S scattering path. Together with a significant fraction of Mo–W coordination, the obtained results confirm the preservation of mixed $MoWS_2$ active phase in the unsupported $Mo_3W_9S_2$ mixed HPA based catalysts suggesting the structure of the active phase after removal of the support.

The above correlates with the ToF-SIMS analysis. The higher amount of mixed sulfide species in MoW HPA based catalyst explains its almost twice higher activity in DBT HDS and naphthalene HYD compared to the bimetallic references. The small amount of mixed Mo–W phase observed in EXAFS for RefMo_3W_9S sample may be explained by partial connection of monometallic MoS_2 and WS_2 slabs to bimetallic ones as schematically illustrated in **Fig. 9b**. However, the efficiency of such particles is still lower, compared to those formed from the mixed precursor. That assumption is in line with the calculated TOF values (**Table 6**) as well as HDS and HYD rate constants which correlated with the relative W–Mo coordination number (**Fig. 10**). Comparing the sample within one supported or unsupported series of catalysts, it can be seen that catalytic activity was increased with an increase of $N_{W\text{-}Mo}$.

5. Conclusions

We found that the HF etching of the alumina in Mo_nW_{12-n}/Al_2O_3 sulfided catalysts led to successful removal of the support. Further interaction between the particles of the etched sulfide active phase after resulfidation of bulk solids resulted to an increase in the average particle length and stacking number, which is independently confirmed by HRTEM, XRD and EXAFS data. The metal sulfidation degree was also raised especially for tungsten, due to removal of non sulfided species. The presence of mixed $MoWS_2$ slabs was confirmed by EXAFS and ToF-SIMS analysis.

A beneficial effect in the catalytic activity of bimetallic unsupported $MoWS_2$ catalysts compared to monometallic MoS_2 and WS_2 ones has been shown. Total DBT HDS and naphthalene

HYD activities were correlated with the Mo-W contribution. Among the prepared bimetallic catalysts, the $Mo_3W_9S_2$ sample synthesized using $H_4SiMo_3W_9O_{40}$ HPA as starting material demonstrated the highest HDS and HYD activities. Together with a significant fraction of Mo–W coordination, the obtained results confirm the preservation of mixed $MoWS_2$ active phase in unsupported $Mo_3W_9S_2$ mixed HPA based catalysts suggesting the structure of the active phase after removal of the support.

Acknowledgments

Authors thank Russian Science Foundation for financial support of the investigation by Grant No. 17-73-20386. Chevreul Institute (FR 2638), Ministère de l'Enseignement Supérieur et de la Recherche, Région Nord – Pas de Calais and FEDER are acknowledged for supporting and funding partially this work (TEM and ToF-SIMS).

References

1. S. Sigurdson, V. Sundaramurthy, A.K. Dalai, J. Adjaye, J. Mol. Catal. A 291 (2008) 30.
2. C. Thomazeau, C. Geantet, M. Lacroix, M. Danot, V. Harlé, P. Raybaud, Appl. Catal. A 322 (2007) 92.
3. H. Yu, S. Li, G. Jin, Energy Fuels 24 (2010) 4419.
4. M. Nikulshina, A. Mozhaev, C. Lancelot, M. Marinova, P. Blanchard, E. Payen, C. Lamonier, P. Nikulshin, Appl. Catal. B 224 (2018) 951.
5. D. Liu, L. Liu, G. Li, C. Liu, J. Nat. Gas Chem. 19 (2010) 530.
6. R. Huirache-Acuña, B. Pawelec, E. Rivera-Muñoz, R. Nava, J. Espino, J.L.G. Fierro, Appl. Catal. B 92 (2009) 168.
7. J.A. Mendoza-Nieto, O. Vera-Vallejo, L. Escobar-Alarcón, D.A. Solís-Casados, T. Klimova, Fuel 110 (2013) 268.

8. M.A. Guzmán, R. Huirache-Acuña, C.V. Loricera, J.R. Hernández, J.N. Díaz de León, J.A. de los Reyes, B. Pawelec, Fuel 103 (2013) 321.
9. M.S. Nikulshina, P. Blanchard, A. Mozhaev, C. Lancelot, A. Griboval-Constant, M. Fournier, E. Payen, O. Mentré, V. Briois, P.A. Nikulshin, C. Lamonier, Catal. Sci. Technol. 8 (2018) 5557.
10. M.S. Nikul'shina, A.V. Mozhaev, P.P. Minaev, M. Fournier, C. Lancelot, P. Blanchard, E. Payen, C. Lamonier, P.A. Nikul'shin, Kinet. Catal. 58 (2017) 825.
11. M. Nikulshina, A. Mozhaev, C. Lancelot, P. Blanchard, M. Marinova, C. Lamonier, P. Nikulshin, Catal. Today 329 (2019) 24.
12. A. Stanislaus, A. Marafi, M.S. Rana, Catal. Today 153 (2010) 1.
13. S. Zhang, D. Liu, W. Deng, G. Que, Energy Fuels. 21 (2007) 3057.
14. G. Bellussi, G. Rispoli, A. Landoni, L. Millini, D. Molinare, E. Montanari, P. Pollesel, J. Catal. 308 (2013) 189.
15. G. Bellussi, G. Rispoli, D. Molinari, A. Landoni, P. Pollesel, N. Panariti, R. Millini, E. Montanari, Catal. Sci. Technol. 3 (2013) 176.
16. M.T. Nguyen, N.T. Nguyen, J. Cho, C. Park, S. Park, J. Jung, C.W. Lee, J. Ind. Eng. Chem. 43 (2016) 1.
17. G. Hagenbach, Ph. Courty, B. Delmon, J. Catal. 31 (1973) 264.
18. R. Candia, B.S. Clausen, H. Topsøe, J. Catal. 77 (1982) 564.
19. M. Zdrazil, Catal. Today 3 (1988) 269.
20. E. Devers, P. Afanasiev, B. Jouguet, M. Vrinat, Catal. Lett. 82 (2002) 13.
21. W.J. Li, E.W. Shi, J.M. Ko, Z.Z. Chen, H. Ogino, T. Fukuda, J. Cryst. Growth. 250 (2003) 418.
22. Y. Peng, Z. Meng, C. Zhong, J. Lu, Z. Yang, Y. Qian, Mater. Chem. Phys. 73 (2002) 327.
23. N. Rueda, R. Bacaud, M. Vrinat, J. Catal. 169 (1997) 404.
24. Y. Li, A. Li, F. Li, D. Liu, Y. Chai, C. Liu, J. Catal. 317 (2014) 240.

25. A.N. Varakin, A.V. Mozhaev, A.A. Pimerzin, P.A. Nikulshin, Appl. Catal. B 238 (2018) 498.
26. S. Kasztelan, H. Toulhoat, J. Grimblot, J.P. Bonnelle, Appl. Catal. 13 (1984) 127.
27. G. Berhault, M.P. De la Rosa, A. Mehta, M.J. Yácaman, R.R. Chianelli, Appl. Catal. A 345 (2008) 80.
28. A. Pimerzin, A. Mozhaev, A. Varakin, K. Maslakov, P. Nikulshin, Appl. Catal. B 205 (2017) 93.
29. S.-H. Kim, K.-D. Kim, Y.-K. Lee, J. Catal. 347 (2017) 127.
30. C.T. Tye, K.J. Smith, Catal. Today 116 (2006) 461.
31. M.P. De la Rosa, J. Catal. 225 (2004) 288.
32. G. Alonso, V. Petranovskii, M. Del Valle, J. Cruz-Reyes, A. Licea-Claverie, S. Fuentes, Appl. Catal. A 197 (2000) 87.
33. K.S. Liang, R.R. Chianelli, F.Z. Chien, S.C. Moss, J. Non-Cryst. 79(3) (1986) 251.
34. B. Guichard, M. Roy-Auberger, E. Devers, C. Pichon, C. Legens, P. Lecour, Catal. Today. 149 (2010) 2.
35. A.V. Mozhaev, P.A. Nikulshin, Al.A. Pimerzin, K.I. Maslakov, A.A. Pimerzin, Catal. Today 271 (2016) 80.
36. A. Cordova, P. Blanchard, C. Lancelot, G. Frémy, C. Lamonier, ACS Catal. 5 (2015) 2966.
37. W. van Beek, O.V. Safonova, G. Wiker, H. Emerich, Phase Transit. 84 (2011) 726.
38. B. Ravel, M. Newville, J. Synchrotron Radiat. 12 (2005) 537.
39. M. Newville, J. Synchrotron Radiat. 8 (2001) 322.
40. R. Huirache-Acuña, M. A. Albiter, C. Ornelas, F. Paraguay-Delgado, R. Martínez-Sánchez, G. Alonso-Nuñez, Appl. Catal. A 308 (2006) 134.
41. L. Alvarez, J. Espino, C. Ornelas, J. L. Rico, M. T. Cortez, G. Berhault, G. Alonso, J. Mol. Catal. A Chem. 210 (2004) 105.

42. J. Bocarando, G. Alonso-Nuñez, W. Bensch, R. Huirache-Acuña, M. Del Valle, J. Cruz-Reyes, Catal. Lett. 130 (2009) 301.
43. L. Álvarez, G. Berhault, G. Alonso-Nuñez, Catal. Lett. 125 (2008) 35.
44. H. Toulhoat, P. Raybaud, J. Catal. 216 (2003) 63.
45. F. Labruyère, M. Lacroix, D. Schweich, M. Breysse, J. Catal. 167 (1997) 464.
46. P. Afanasiev, Appl. Catal. A 303 (2006) 110.
47. B. Yoosuk, D. Tumnantong, P. Prasassarakich, Chem. Eng. Sci. 79 (2012) 1.
48. M. Elizabeth, C. Gaxiola, M. Arroyo-Albiter, A. Pérez-Larios, P.B. Balbuena, J. Espino-Valencia, Fuel 113 (2013) 733.
49. L. Kaluža, M. Zdražil, Catal. Commun. 107 (2018) 62.
50. J.N. Díaz de León, J. Antunes-García, G. Alonso-Nuñez, T.A. Zepeda, D.H. Galvan, J.A. de los Reyes, S. Fuentes, Appl. Catal. B 238 (2018) 480.
51. L. Kaluža, M. Koštejn, D. Gulková, Catalysts 9 (12) (2019) 987.
52. M. Kniazeva, A. Maximov, Catalysts 2018 8(12) 644.

Captions for Tables

Table 1. Composition and textural properties of prepared unsupported $Mo_nW_{12-n}S_2$ catalysts.

Table 2. Quantitative H_2-TPR results of unsupported $Mo_nW_{12-n}S_2$ catalysts.

Table 3. Morphological characteristics of $Mo_nW_{12-n}S_2$ active phase species calculated from TEM micrographs and XRD.

Table 4. Metal fractions measured by XPS for molybdenum and tungsten species present in unsupported $Mo_nW_{12-n}S_2$ catalysts.

Table 5. Structural parameters obtained from the Fourier-analysis of Mo *K*- and W L_3-edges EXAFS spectra of unsupported $Mo_nW_{12-n}S_2$ catalysts. The values in brackets correspond to the supported catalysts. The values for W–Mo scattering path given without the uncertainty were linked to the values for Mo–W path.

Table 6. Catalytic properties of prepared unsupported $Mo_nW_{12-n}S_2$ catalysts in HDT of a mixture of DBT and naphthalene.

Captions for Figures

Figure 1. H_2-TPR profiles for unsupported $Mo_nW_{12-n}S_2$ catalysts.

Figure 2. HRTEM micrographs of unsupported $Mo_nW_{12-n}S_2$ catalysts.

Figure 3. XRD patterns of unsupported $Mo_nW_{12-n}S_2$ catalysts.

Figure 4. XPS Mo 3d and W 4f spectra recorded for unsupported $Mo_nW_{12-n}S_2$ catalysts; in blue: $Mo(W)^{6+}$ oxide contributions; in pink: $Mo(W)S_xO_y$ contributions; in gray: $Mo(W)S_2$ contributions (For interpretation of the references to color in this figure legend, the reader should refer to the web version of the article).

Figure 5. Phase-uncorrected Fourier transformed Mo *K*- (a) and W L_3- (b) edges k^3-weighted EXAFS data for unsupported monometallic (blue lines) and bimetallic (red lines) catalysts. Green lines correspond to the sample prepared from the mixture of monometallic HPAs. Dashed lines correspond to the data for similar supported catalysts reported in [9]. Corresponding $\chi(k)$ signals are shown in Figure S2 of the Supporting Information.

Figure 6. Mass spectra obtained by TOF-SIMS analysis of unsupported MoS_2, WS_2, $Mo_3W_9S_2$ and $RefMo_3W_9S_2$ catalysts

Figure 7. Fragments contribution on unsupported $Mo_nW_{12-n}S_2$ catalysts.

Figure 8. Rate constants of DBT HDS (a) and naphthalene HYD (b) over unsupported $Mo_nW_{12-n}S_2$ and supported Mo_nW_{12-n}/Al_2O_3 [9] catalysts.

Figure 9. The possible simplified model of mixed $MoWS_2$ active particles in unsupported $Mo_3W_9S_2$ (a) and $RefMo_3W_9S_2$ (b) catalysts.

Figure 10. Activity in DBT HDS (a) and naphthalene HYD (b) over unsupported $Mo_nW_{12-n}S_2$ and supported Mo_nW_{12-n}/Al_2O_3 [9] catalysts depending on the W-Mo coordination number.

Table 1

Composition and textural properties of prepared unsupported $Mo_nW_{12-n}S_2$ catalysts.

Catalyst	Content in the catalyst (wt. %)		Mo/W atomic ratio [a]	S/(Mo+W)	Specific surface area (m^2/g)	Pore volume (cm^3/g)	Average pore diameter (nm)
	C	S					
MoS_2	2.0	35.0	-	1.8	8 / 210 [b]	0.04 / 0.57 [b]	< 3.8 / 7.2 [b]
WS_2	1.2	25.3	-	2.2	14 / 164	0.03 / 0.48	< 3.8 / 7.9
$Mo_1W_{11}S_2$	1.4	27.2	0.15	2.2	5 / 218	0.01 / 0.56	< 3.8 / 6.8
$Mo_3W_9S_2$	1.9	29.4	0.55	2.0	5 / 179	0.01 / 0.51	< 3.8 / 6.8
$RefMo_1W_{11}S_2$	1.5	28.1	0.20	2.2	10 / 182	0.03 / 0.51	< 3.8 / 7.2
$RefMo_3W_9S_2$	1.0	30.4	0.60	2.1	3 / 190	0.04 / 0.55	< 3.8 / 7.9

[a] XRF analysis; [b] Values for supported sulfided Mo_nW_{12-n}/Al_2O_3 catalysts.

Table 2

Quantitative H_2-TPR results of unsupported $Mo_nW_{12-n}S_2$ catalysts

Catalyst	1st peak		2nd peak		3rd peak		Total H_2 cons.
	T_{max} (ºC)	H_2 cons. (mmol/mol M)	T_{max} (ºC)	H_2 cons. (mmol/mol M)	T_{max} (ºC)	H_2 cons. (mmol/mol M)	(mmol/mol M)
MoS_2	303 / 343*	715 /1453*	-	-	-	-	715
WS_2	342 / 259	230 / 99	461	604	674	60	895
$Mo_1W_{11}S_2$	334 / 255	390 / 247	506	232	-	-	622
$Mo_3W_9S_2$	319 / 263	640 / 258	514	174	-	-	813
$RefMo_1W_{11}S_2$	378 / 252	367 / 180	503	379	-	-	746
$RefMo_3W_9S_2$	339 / 269	450 / 330	515	202	-	-	670

* Values for supported sulfided Mo_nW_{12-n}/Al_2O_3 catalysts.

Table 3

Morphological characteristics of $Mo_nW_{12-n}S_2$ active phase species calculated from TEM micrographs and XRD.

Catalyst	Average length $\bar{L}$ (nm)		Average stacking number $\overline{N}$		Dispersion of $Mo_nW_{12-n}S_2$ D^b	Distribution of slab length (rel. %)					Distribution of stacking number (rel. %)			
						<2	2..4	4..6	6..8	>8	1	2	3	>3
MoS_2	5.2[a]	6.3[b]	3.3[a]	4.2[b]	0.19	3	34	34	15	14	14	17	25	44
WS_2	6.7	9.6	3.5	4.8	0.13	1	32	23	18	26	6	16	30	48
$Mo_1W_{11}S_2$	5.5	7.8	3.1	4.4	0.16	1	26	37	23	13	11	25	29	35
$Mo_3W_9S_2$	5.2	7.9	3.0	4.5	0.16	4	96	-	-	-	14	29	22	35
$RefMo_1W_{11}S_2$	4.9	7.9	3.0	4.5	0.16	2	32	44	18	4	8	32	26	34
$RefMo_3W_9S_2$	4.8	6.5	3.1	4.2	0.19	3	97	-	-	-	7	29	27	37

[a] Obtained from TEM analysis; [b] from XRD data.

Table 4

Metal fractions measured by XPS for molybdenum and tungsten species present in unsupported $Mo_nW_{12-n}S_2$ catalysts.

Catalyst	Mo/W at. ratio	S/(Mo+W)	Mo fraction (rel. %)			W fraction (rel. %)		
			MoS_2	MoS_xO_y	Mo^{6+}	WS_2	WS_xOy	W^{6+}
MoS_2	-	1.8	92	5	3	-	-	-
WS_2	-	2.2	-	-	-	92	4	4
$Mo_1W_{11}S_2$	0.16	2.2	98	2	0	92	4	4
$Mo_3W_9S_2$	0.57	2.0	93	3	4	95	2	3
$RefMo_1W_{11}S_2$	0.22	2.2	94	5	1	94	3	3
$RefMo_3W_9S_2$	0.68	2.1	92	4	4	95	2	3

Table 5

Structural parameters obtained from the Fourier-analysis of Mo *K*- and W L_3-edges EXAFS spectra of unsupported $Mo_nW_{12-n}S_2$ catalysts. The values in brackets correspond to the supported catalysts. The values for W–Mo scattering path given without the uncertainty were linked to the values for Mo–W path.

Scattering path	*N*	*R* (Å)	$\sigma^2 \cdot 10^3$ (Å²)	ΔE_0 (eV)	*R*-factor
			MoS_2		
Mo–S	5.3 ± 0.2	2.41 ± 0.01	4.1 ± 0.3		
	(6.1 ± 0.2)	(2.41 ± 0.01)	(4.3 ± 0.2)	1.4 ± 0.4	0.0023
Mo–Mo	3.7 ± 0.4	3.16 ± 0.01	4.9 ± 0.5	(2.5± 0.4)	(0.0016)
	(3.9 ± 0.4)	(3.17 ± 0.01)	(5.3 ± 0.5)		
			WS_2		
W–S	5.3 ± 0.4	2.41 ± 0.01	2.4 ± 0.5		
	(4.5 ± 0.3)	(2.41 ± 0.01)	(3.0 ± 0.5)	8.8 ± 1.0	0.0115
W–W	4.4 ± 1.0	3.16 ± 0.01	3.3 ± 0.7	(8.7± 1.1)	(0.0133)
	(3.9 ± 0.4)	(3.16 ± 0.01)	(4.0 ± 1.0)		
			$Mo_3W_9S_2$		
Mo–S	5.8 ± 0.4	2.41 ± 0.01	3.4 ± 0.6		
	(6.0 ± 0.4)	(2.42 ± 0.01)	(3.8 ± 0.7)		
Mo–Mo	3.4 ± 1.5	3.16 ± 0.01	4.9 ± 2.6	2.6 ± 1.0	
	(1.9 ± 1.3)	(3.17 ± 0.02)	(3.9 ± 3.9)	(2.4 ± 1.1)	
Mo–W	2.8 ± 2.0	3.17 ± 0.03	6.3 ± 4.2		0.0116
	(2.6 ± 1.5)	(3.18 ± 0.02)	(4.6 ± 3.1)		(0.0063)
W–S	5.2 ± 0.4	2.41 ± 0.01	3.1 ± 0.6		
	(5.3 ± 0.2)	(2.41 ± 0.01)	(3.7 ± 0.4)	8.2 ± 1.2	
W–W	2.8 ± 1.2	3.16 ± 0.01	4.1 ± 1.5	(8.9 ± 0.8)	
	(2.4 ± 0.8)	(3.17 ± 0.01)	(4.3 ± 1.1)		
W–Mo	0.9 (0.9)	3.17 (3.18)	6 (5)		
			Reference $Mo_3W_9S_2$		
Mo–S	5.8 ± 0.4	2.41 ± 0.01	3.5 ± 0.5		
	(6.0 ± 0.5)	(2.42 ± 0.01)	(3.8 ± 0.8)		
Mo–Mo	3.6 ± 1.2	3.16 ± 0.01	4.2 ± 1.9	2.5 ± 0.9	
	(3.0 ± 1.5)	(3.17 ± 0.01)	(4.2 ± 2.9)	(2.9 ± 1.2)	
Mo–W	2.0 ± 1.7	3.16 ± 0.03	6.0 ± 5.1		0.0148
	(1.6 ± 1.3)	(3.18 ± 0.02)	(3.6 ± 4.0)		(0.0056)
W–S	4.8 ± 0.3	2.41 ± 0.01	2.4 ± 0.5		
	(5.1 ± 0.2)	(2.41 ± 0.01)	(3.4 ± 0.4)	7.6 ± 1.1	
W–W	2.8 ± 1.0	3.16 ± 0.01	3.6 ± 1.2	(8.8 ± 0.8)	
	(2.4 ± 0.7)	(3.17 ± 0.01)	(3.8 ± 1.1)		
W–Mo	0.7 (0.5)	3.16 3.18)	6 (4)		

Table 6

Catalytic properties of prepared unsupported $Mo_nW_{12-n}S_2$ catalysts in HDT of a mixture of DBT and naphthalene.

Catalyst	Conversion (%)		Selectivity ratio in	Rate constants ($\times 10^5$ mol g^{-1} h^{-1})		*TOF* values ($\times 10^4$ s^{-1})	
	DBT HDS	Naphthalene HYD	DBT HDS $S_{HYD/DDS}$	k_{HDS}	k_{HYD}	TOF_{HDS}	TOF_{HYD}
MoS_2	22	14	1.0	60	179	1.5	4.7
WS_2	24	15	1.7	66	198	3.8	12.0
$Mo_1W_{11}S_2$	31	20	2.8	90 / 65*	277 / 196*	3.8 / 3.6*	12.4 / 11.4*
$Mo_3W_9S_2$	50	35	2.6	171 / 64	523 / 193	6.0 / 3.2	20.9 / 10.2
$RefMo_1W_{11}S_2$	34	18	1.7	100 / 65	240 / 196	4.0 / 3.6	10.6 / 11.4
$RefMo_3W_9S_2$	29	18	2.6	85 / 64	243 / 193	2.7 / 3.2	8.3 / 10.2

*The additive quantities, which were calculated using the values for monometallic MoS_2 and WS_2.

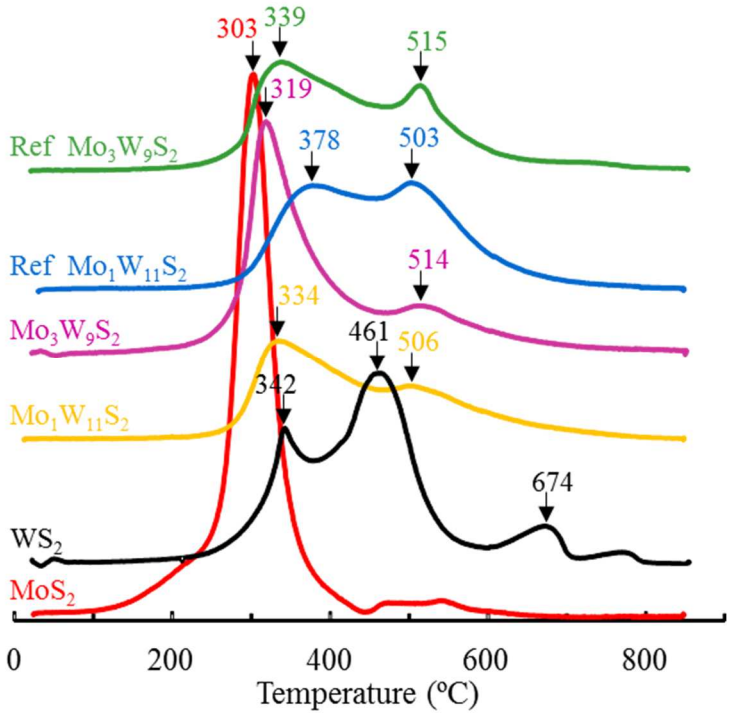

Fig. 1. H_2-TPR profiles for unsupported $Mo_nW_{12-n}S_2$ catalysts.

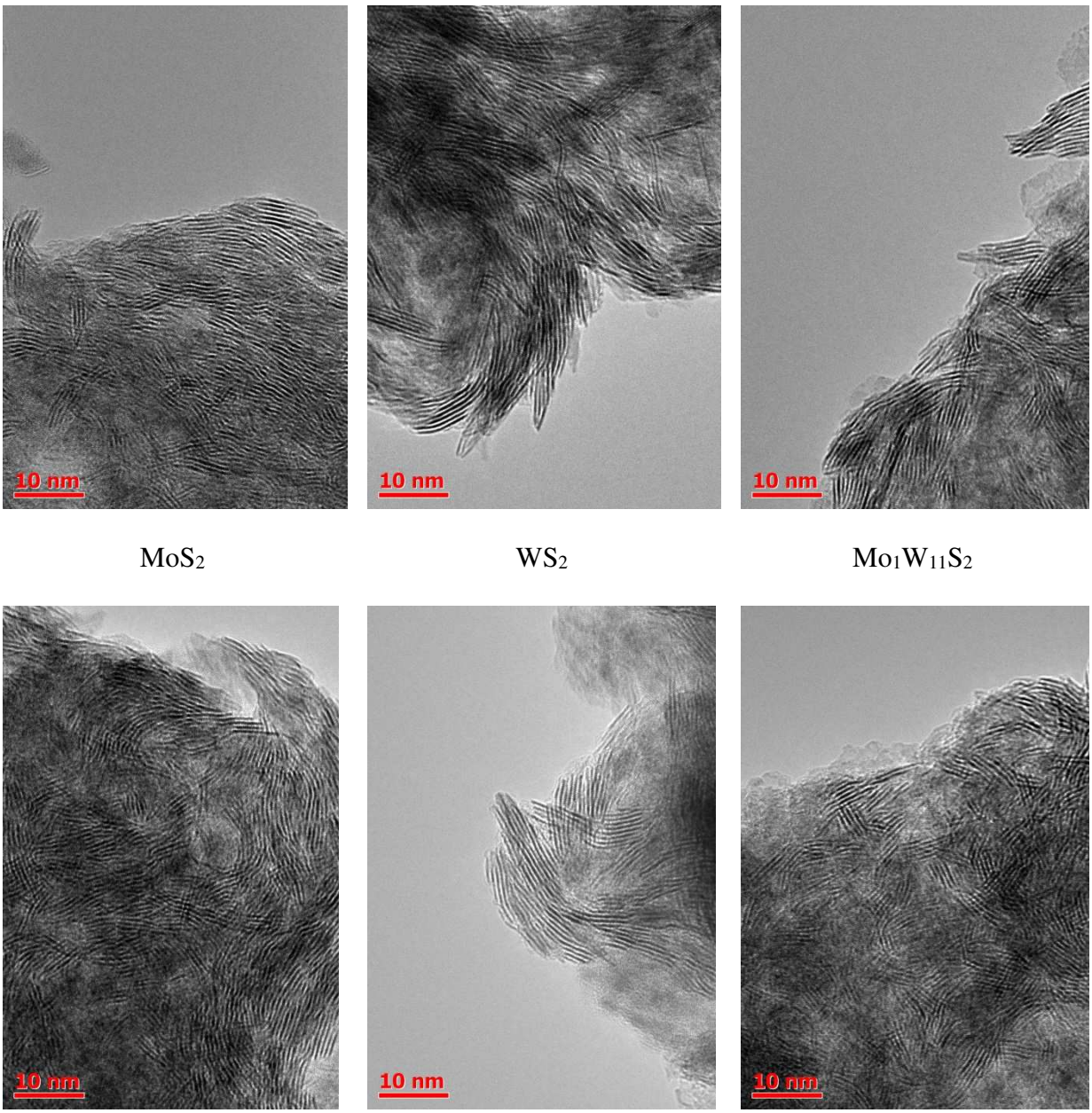

MoS_2 WS_2 $Mo_1W_{11}S_2$

$Mo_3W_9S_2$ $RefMo_1W_{11}S_2$ $RefMo_3W_9S_2$

Fig. 2. HRTEM micrographs of unsupported $Mo_nW_{12-n}S_2$ catalysts.

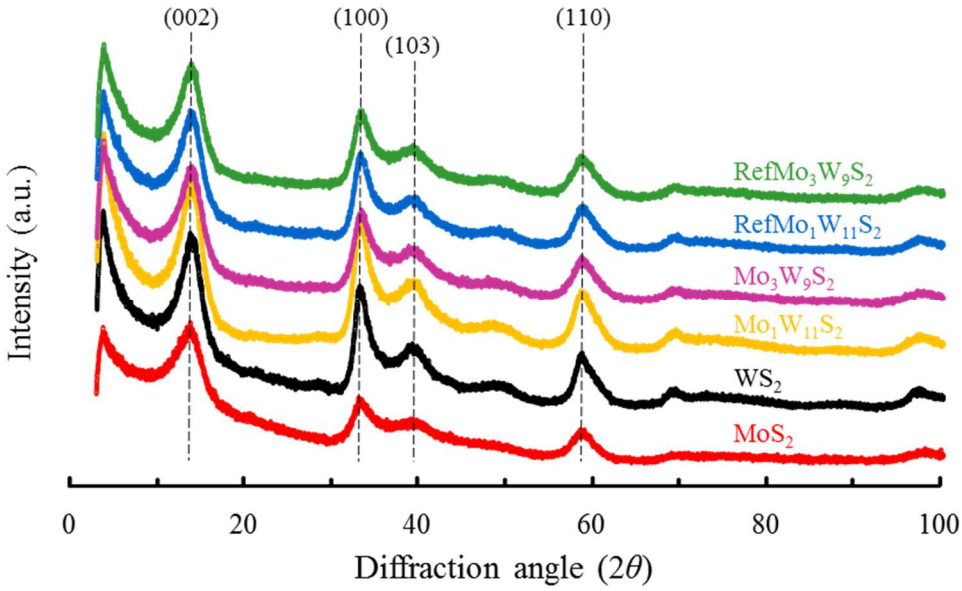

Fig. 3. XRD patterns of unsupported $Mo_nW_{12-n}S_2$ catalysts.

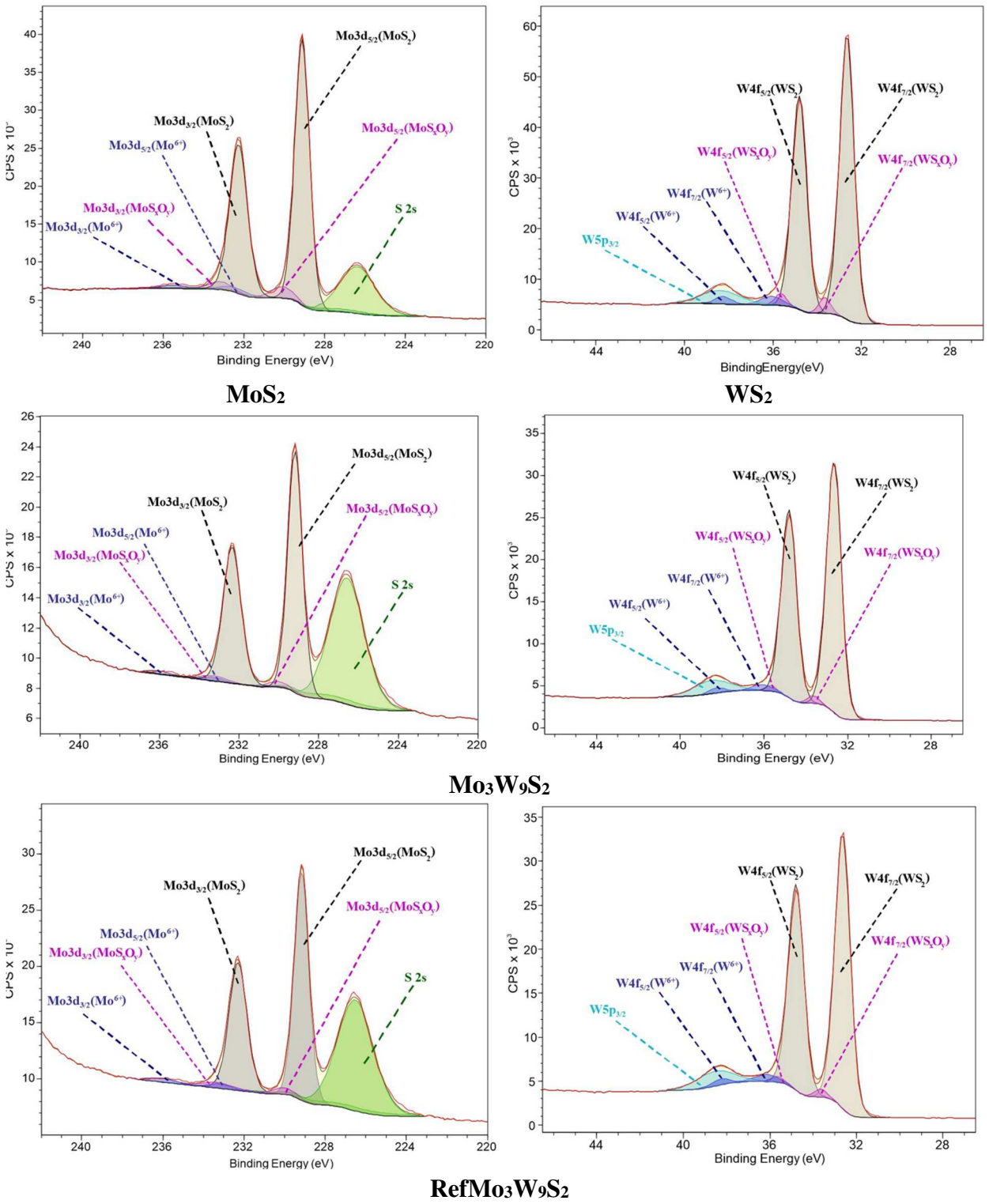

Fig. 4. XPS Mo 3d and W 4f spectra recorded for unsupported $Mo_nW_{12-n}S_2$ catalysts; in blue: $Mo(W)^{6+}$ oxide contributions; in pink: $Mo(W)S_xO_y$ contributions; in gray: $Mo(W)S_2$ contributions (For interpretation of the references to color in this figure legend, the reader should refer to the web version of the article).

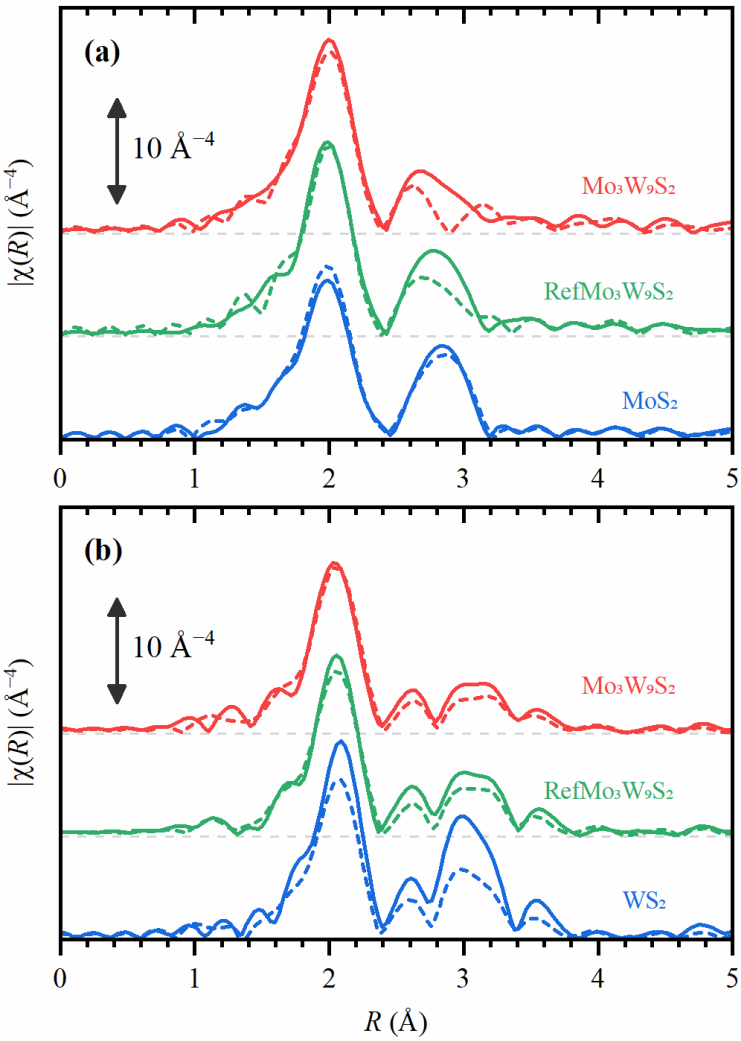

Fig. 5. Phase-uncorrected Fourier transformed Mo *K*- (a) and W L_3- (b) edges k^3-weighted EXAFS data for unsupported monometallic (blue lines) and bimetallic (red lines) catalysts. Green lines correspond to the sample prepared from the mixture of monometallic HPAs. Dashed lines correspond to the data for similar supported catalysts reported in [9]. Corresponding χ(*k*) signals are shown in Figure S2 of the Supporting Information.

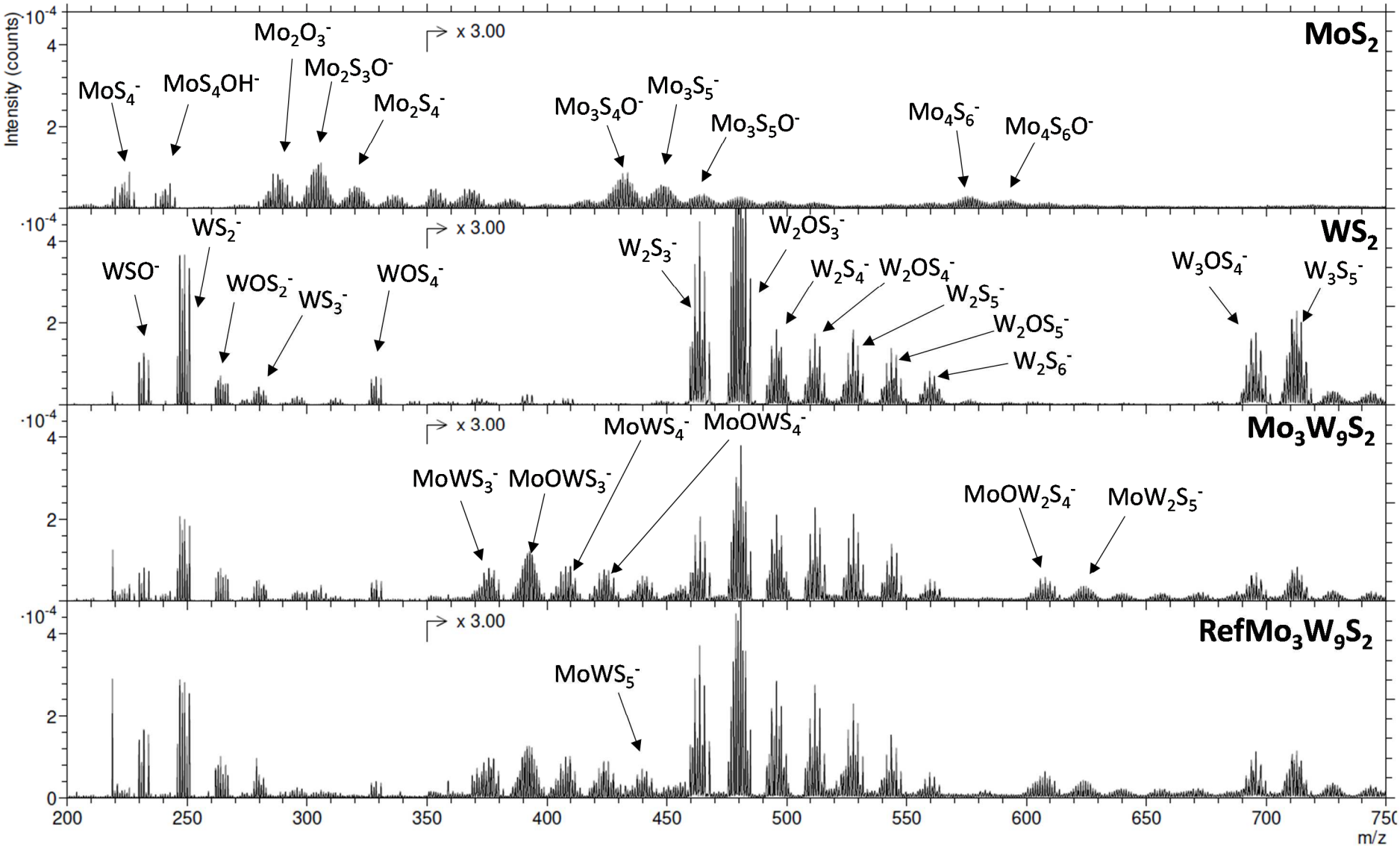

Fig. 6. Mass spectra obtained by TOF-SIMS analysis of unsupported MoS_2, WS_2, $Mo_3W_9S_2$ and $RefMo_3W_9S_2$ catalysts.

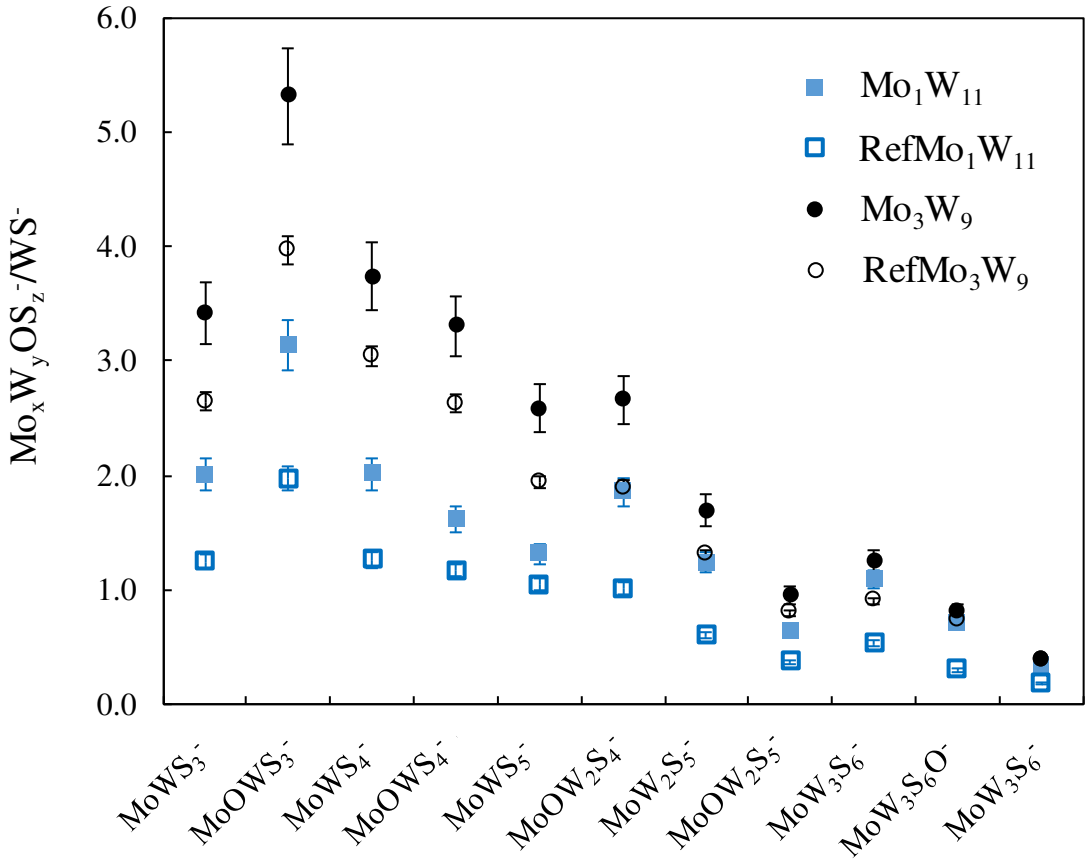

Fig. 7. Fragments contribution on unsupported $Mo_nW_{12-n}S_2$ catalysts.

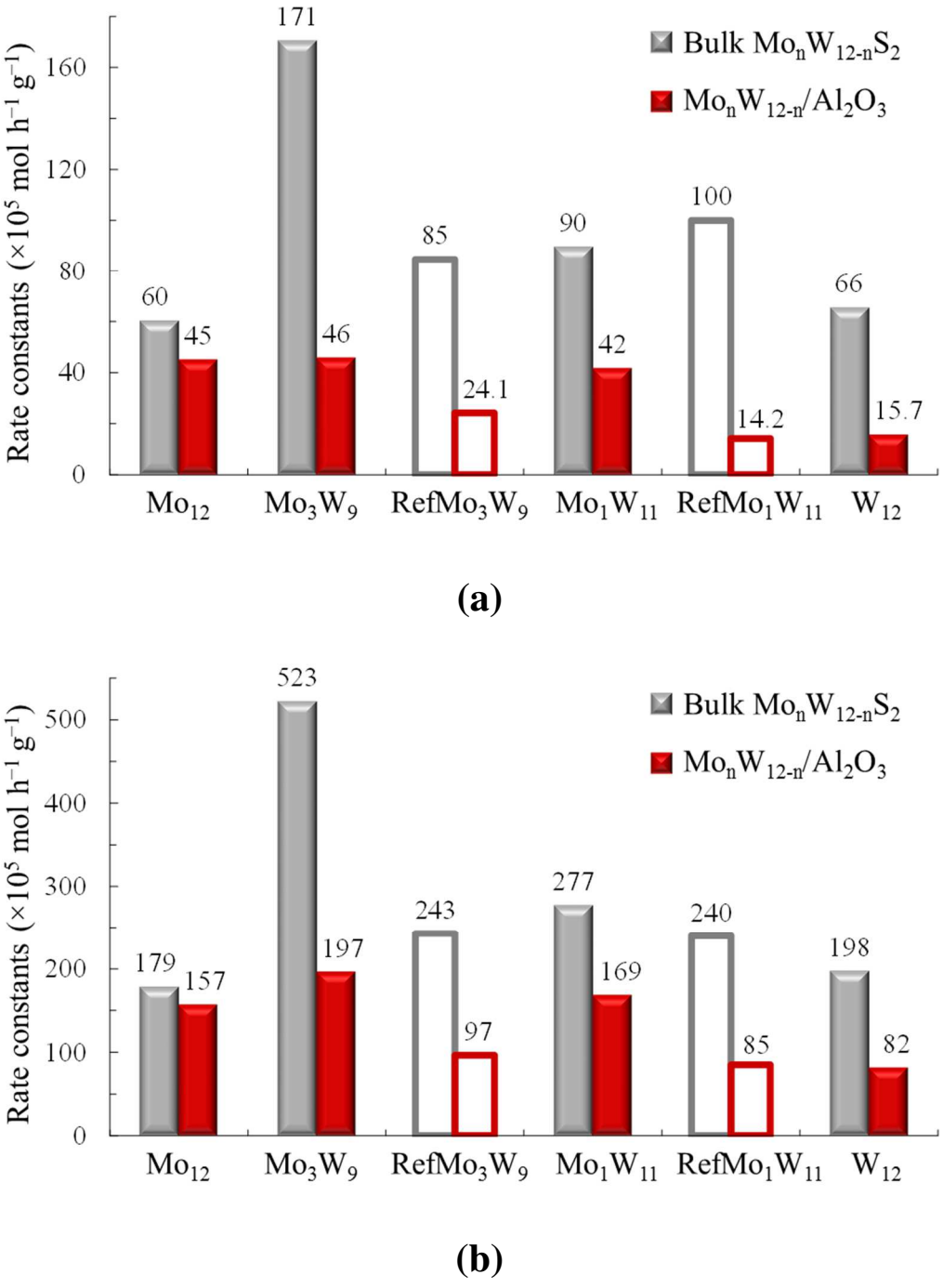

Fig. 8. Rate constants of DBT HDS (a) and naphthalene HYD (b) over unsupported $Mo_nW_{12-n}S_2$ and supported Mo_nW_{12-n}/Al_2O_3 [9] catalysts.

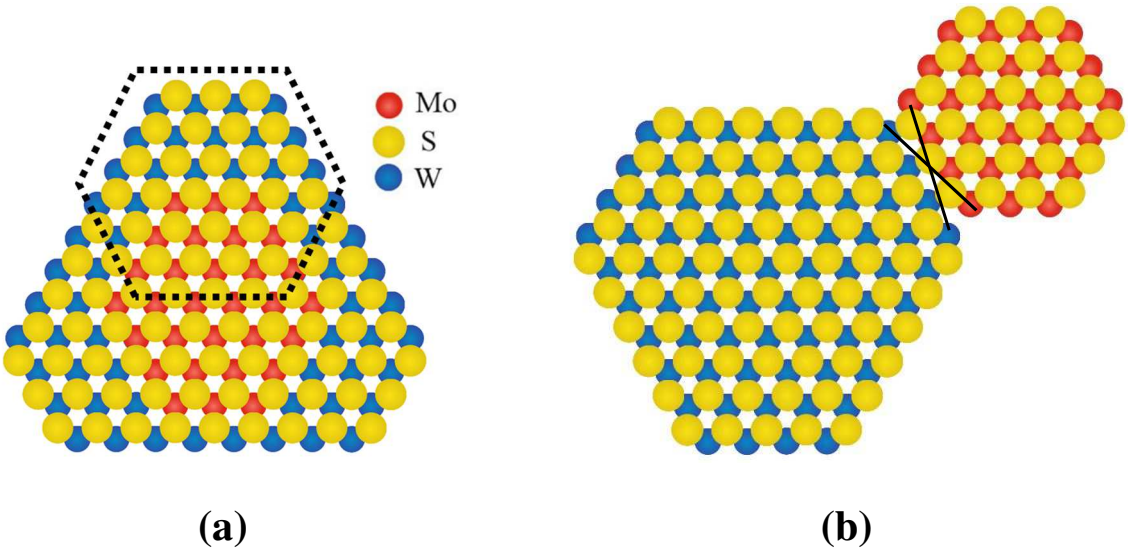

Fig. 9. The possible simplified models of mixed $MoWS_2$ active particles in unsupported $Mo_3W_9S_2$ (a) and Ref$Mo_3W_9S_2$ (b) catalysts.

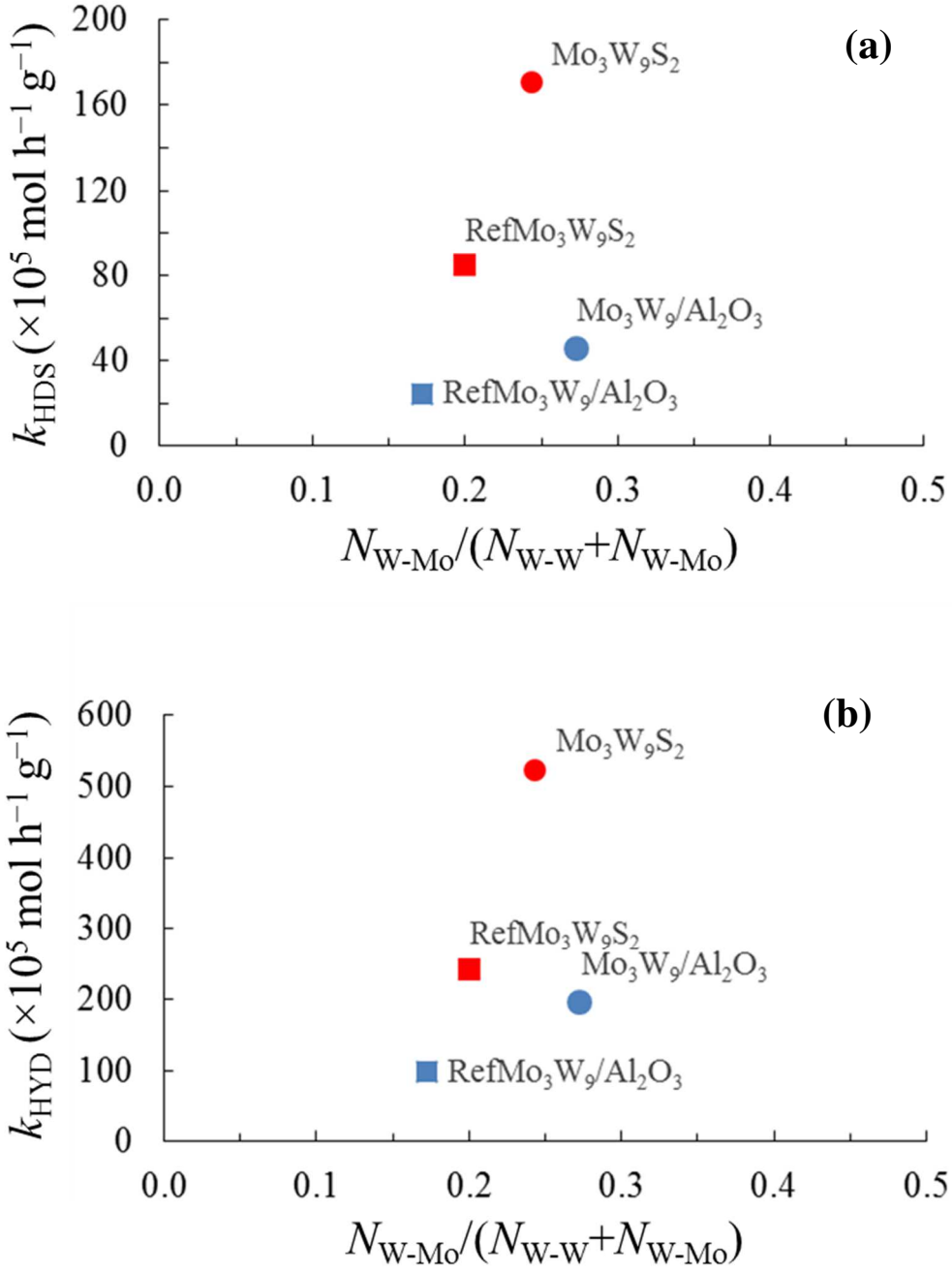

Fig. 10. Activity in DBT HDS (a) and naphthalene HYD (b) over unsupported $Mo_nW_{12-n}S_2$ and supported Mo_nW_{12-n}/Al_2O_3 [9] catalysts depending on the W-Mo coordination.